



Article

Arctic Thin Ice Detection Using AMSR2 and FY-3C MWRI Radiometer Data

Marko Mäkynen * and Markku Similä

Finnish Meteorological Institute, P.O. Box 503, FI-00101 Helsinki, Finland

* Correspondence: marko.makynen@fmi.fi

Abstract: Thin ice with a thickness of less than half a meter produces strong salt and heat fluxes which affect deep water circulation and weather in the polar oceans. The identification of thin ice areas is essential for ship navigation. We have developed thin ice detection algorithms for the AMSR2 and FY-3C MWRI radiometer data over the Arctic Ocean. Thin ice (<20 cm) is detected based on the classification of the H-polarization 89–36-GHz gradient ratio (GR8936H) and the 36-GHz polarization ratio (PR36) signatures with a linear discriminant analysis (LDA) and thick ice restoration with GR3610H. The brightness temperature (T_B) data are corrected for the atmospheric effects following an EUMETSAT OSI SAF correction method in sea ice concentration retrieval algorithms. The thin ice detection algorithms were trained and validated using MODIS ice thickness charts covering the Barents and Kara Seas. Thin ice detection is applied to swath T_B datasets and the swath charts are compiled into a daily thin ice chart using 10 km pixel size for AMSR2 and 20 km for MWRI. On average, the likelihood of misclassifying thick ice as thin in the ATIDA2 daily charts is 7.0% and 42% for reverse misclassification. For the MWRI chart, these accuracy figures are 4% and 53%. A comparison of the MWRI chart to the AMSR2 chart showed a very high match (98%) for the thick ice class with SIC > 90% but only a 53% match for the thin ice class. These accuracy disagreements are due to the much coarser resolution of MWRI, which gives larger spatial averaging of T_B signatures, and thus, less detection of thin ice. The comparison of the AMSR2 and MWRI charts with the SMOS sea ice thickness chart showed a rough match in the thin ice versus thick ice classification. The AMSR2 and MWRI daily thin ice charts aim to complement SAR data for various sea ice classification tasks.

Keywords: Arctic; passive microwave remote sensing; polynya; thin sea ice



Citation: Mäkynen, M.; Similä, M. Arctic Thin Ice Detection Using AMSR2 and FY-3C MWRI Radiometer Data. *Remote Sens.* **2024**, *16*, 1600. <https://doi.org/10.3390/rs16091600>

Academic Editors: Qingyun Yan, Linlin Xu and Xinwei Chen

Received: 19 February 2024

Revised: 19 April 2024

Accepted: 28 April 2024

Published: 30 April 2024



Copyright: © 2024 by the authors. Licensee MDPI, Basel, Switzerland. This article is an open access article distributed under the terms and conditions of the Creative Commons Attribution (CC BY) license (<https://creativecommons.org/licenses/by/4.0/>).

1. Introduction

During the winter months in the Arctic Ocean, the formation of thin sea ice occurs not only along the ice edge but also within leads and polynyas amidst pack ice. Additionally, in the marginal ice zone (MIZ) a vast expansion of thin ice takes place during the sea ice freeze-up period. Thin ice, with a thickness under half a meter, is responsible for significant salt and thermal fluxes, impacting the circulation of deep ocean currents and atmospheric conditions in the polar areas. Accurately identifying thin ice regions is also crucial for navigating ships through icy waters.

Thin ice detection and ice thickness (h_i) retrieval in winter conditions can be performed with microwave radiometer data. L-band brightness temperature (T_B) data from the Soil Moisture and Ocean Salinity (SMOS) satellite are applicable to estimate h_i up to 1.5 m [1–4]. However, the detection of smaller polynyas and leads is hampered by the relatively low spatial resolution of the T_B data, ranging from 35 km to 50 km.

Ice formation and thickening in polynyas have been the subject of several studies that utilize high-frequency channels (near 36 and 90 GHz) of radiometer data [5–12]. There are detailed reviews of these studies in [9,13]. The h_i retrieval algorithms are mostly exponential regression equations between polarization ratio (PR) at 36 or 90 GHz and h_i derived from T_S in thermal infrared imagery. PR gives an indirect h_i estimate through

the surface salinity of thin ice. On average, the surface salinity decreases with increasing h_i , leading to a decrease in PR [14,15]. The maximum estimated thin ice h_i has typically been 20 cm [6,8,9,16,17]. Atmospheric factors like cloud liquid water and water vapor can significantly lower PR90, potentially leading to an overestimation of h_i [6]. Contaminated PR90 pixels are usually flagged and only PR36 is used for the h_i retrieval. The minimum sea ice concentration (SIC) for the h_i estimation has usually been set to 15% or 30%. The uncertainty of the estimated h_i has been assessed to be from 5 to 8 cm when characterized by the root-mean-square difference (RMSD) [7,8,10,16–18]. The PR36 and PR90 based h_i data have been used to track Antarctic and Arctic polynyas in terms of their occurrence, size, ice production, and temporal trends, e.g., [7–9,11,12].

Only the detection of thin ice (thickness < 30 cm) has been also conducted. Notably, the polynya signature simulation method (PSSM) integrates the high spatial resolution of 90 GHz with the reduced atmospheric impact at 36 GHz to differentiate between first-year ice (FYI), thin ice, and open water, achieving a resolution of 5 km and producing maps indicating polynyas or ice edges [19,20]. The discrimination between thin ice and FYI is sensitive on the chosen tie points for these ice types. An algorithm for detecting leads using daily average T_B data from the Advanced Microwave Scanning Radiometer–Earth Observing System (AMSR-E) have been created in [21]. The utilized statistic is the V-polarization ratio between T_B 's at 89 and 18.7 GHz (T_{B89V}/T_{B18V}). The method was developed and validated with MODIS (Moderate Resolution Imaging Spectroradiometer) imagery. It identifies leads over 3 km wide, detecting at least half of those visible in MODIS imagery and is applicable in areas with dense sea ice (>90%) during Arctic winter.

Recently, we introduced an algorithm for detecting thin ice (thickness < 0.2 m) in the Arctic Ocean using AMSR2 (Advanced Microwave Scanning Radiometer 2) radiometer data [13]. This algorithm, denoted as ATIDA2 (AMSR2 Thin Ice Detection Algorithm—Version 2), is an improved version of the original ATIDA algorithm [22]. It employs linear discrimination analysis (LDA) to classify PR36 and H-polarization 89–36 GHz gradient ratio (GR) signatures, along a process for correcting misidentified thick ice instances using GR3610H, a new feature that is not present in the original ATIDA. This correction step is essential for eliminating incorrect thin ice detections due to the signature mixing between thin and thick ice. The ATIDA2 algorithm is used solely under conditions where sea ice concentration (SIC) is above 70% and air temperature T_a is below $-5\text{ }^\circ\text{C}$ to limit the misidentification of thick ice as thin ice. The algorithm processes AMSR2 L1R T_B swath data [23], aggregating the outcomes into a daily chart of thin ice. For the T_B data, an atmospheric correction is applied following an EUMETSAT OSI SAF (Ocean and Sea Ice Satellite Application Facility) correction method in SIC retrieval algorithms [24–26]. Adjustments to PR and GR signatures based on T_a , standardized to $-25\text{ }^\circ\text{C}$ address the slight increases observed with rising T_a . The daily charts exhibit an 8.7% average risk of mistaking thick ice for thin and a 37.0% risk for the reverse. A comparative analysis of the ATIDA2 charts with SMOS ice thickness data reveals a general alignment in the differentiation of thin ice versus thick ice categories. Aimed at complementing SAR imagery for sea ice classification, ATIDA2 is tuned to significantly reduce the risk of misclassifying thick ice as thin, a critical factor in maritime navigation.

Unfortunately, several error sources persist in the detection and thickness estimation of thin ice using radiometer data, including the mixing of T_B signatures from different surfaces (open water, thin ice, FYI, and landfast ice) due to the coarse resolution of radiometers. Such mixing can, for example, make thick ice with low SIC appear similar to thin ice near 100% SIC. Although setting a higher SIC threshold for detecting thin ice may reduce this feature, SIC for thin ice is often underestimated [25,27–29]. The physical characteristics of thin ice, including surface roughness and the presence of frost flowers or a dry snow layer, can lead to T_B signatures similar to those of much thicker ice [14,30–32]. Atmospheric interference in T_B data also poses a risk of overestimating thin ice thickness [6] or falsely detecting thin ice. In spite of these error sources, many studies have demonstrated thin ice detection and its thickness estimation with sufficient accuracy [7,9,12,13,20,21].

In this study, we improve the T_B atmospheric correction and determine an ATIDA2-like algorithm for the FY-3C (FengYung 3C) MWRI (Micro-Wave Radiation Imager) T_B data that has a much coarser resolution than the AMSR2 data. The specific objectives of our study are the following. (1) Enhance the atmospheric correction of the T_B data. (2) Re-determine ATIDA2 for the AMSR2 T_B data with the new T_B atmospheric correction. (3) Determine the MWRI thin ice detection algorithm (MTIDA2) using MWRI T_B data corrected with the same atmospheric correction method as for the AMSR2 data. (4) Calculate ATIDA2 and MTIDA2 charts over the Arctic for one winter season, October 2016–May 2017, and investigate their statistical similarities and differences. (5) Compare ATIDA2 and MTIDA2 Arctic charts against the SMOS h_i chart. MODIS ice thickness charts over the Barents and Kara Seas were chosen to be used in the learning and evaluation of ATIDA2 and MTIDA2. They were the only data source of thin ice thickness available in fine resolution. The SMOS h_i chart is the operational validated source of thin ice thickness data.

The AMSR2 and MWRI daily thin ice charts are intended to complement SAR data in various sea ice classification tasks. Previously, we have used AMSR2 thin ice chart in conjunction with SAR and sea ice modeling data for ship navigation purposes [33]. In addition, the updated charts can indicate the presence of thin ice in the SIC and snow depth estimation for either pixel flagging or corrective actions.

2. Materials

Datasets used in this study are described below. Many datasets originate from our earlier studies in [13,22] and, therefore, they are described here only shortly.

2.1. MODIS Ice Thickness Charts

MODIS ice thickness (h_{iM}) swath charts over the Barents and Kara Seas (BKS) are used in the learning and evaluation of ATIDA2 and MTIDA2 algorithms and MODIS h_{iM} daily charts, also over BKS, in the validation of the daily thin ice charts, see examples in Figures 1 and 2. The processing methods of the h_{iM} swath chart are detailed in [22,34] and those of the h_{iM} daily chart in [35]. The h_{iM} retrieval is carried out only when air temperature, T_a , according to the ERA5 reanalysis data, is below -5 °C due to high uncertainty in warmer temperatures. The daily chart is calculated from cloud-masked swath h_{iM} charts. The swath charts cover the time periods January–April 2014 and October 2014–April 2015 and their total number is 173. The daily charts cover two winters, November–April in 2015–2017, and there are in total 317 charts. The charts are in a polar stereographic (PS) coordinate system with true-scale latitude of 70N, mid-longitude of 55E, and grid size of 1 km and have a coverage of 1850 km (northing) by 2200 km (easting). The cloud masking for the h_{iM} swath charts during the 2014–2015 season utilizes both manual and automated techniques [34], whereas only automated procedures are applied in the cloud masking of the swath charts processed to the daily charts, with the cloud mask resolution set at 10 km [35]. The cloud mask is composed of the original 1 km mask by flagging a 10×10 km block cloudy if there were more than 10% cloudy 1 km pixels.

The thickness values in the swath h_{iM} chart range from 0 to 1 m, with a resolution of 0.01 m. Ice thickness estimates exceeding 1 m or those yielding negative values (indicating a failure in estimation) are flagged as 1 m and -0.1 m, respectively. The daily h_{iM} chart shows the daily median h_{iM} calculated from at least two samples. It consists of pixelwise h_{iM} values of 0–0.3 m for thin ice, 0.4 m to represent ice thicknesses between 0.31 and 0.5 m (corresponding to the initial stage of thin FYI) [36], and 0.5 m for ice with h_i exceeding 0.5 m.

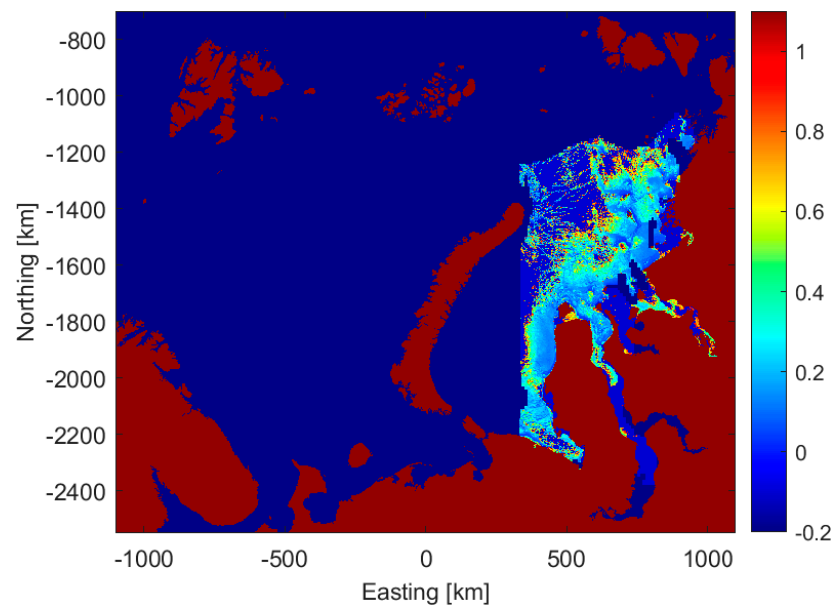


Figure 1. MODIS ice thickness swath chart derived from the ice surface temperature data acquired on 6 December 2014, 06:35 UTC. Dark blue is either cloud mask (thickness -0.2 m), no data mask (-0.3 m), or scan angle larger than 40° (-0.2 m) and light blue (-0.1 m) indicates areas where ice thickness retrieval was unsuccessful. Pixel size is 1 km.

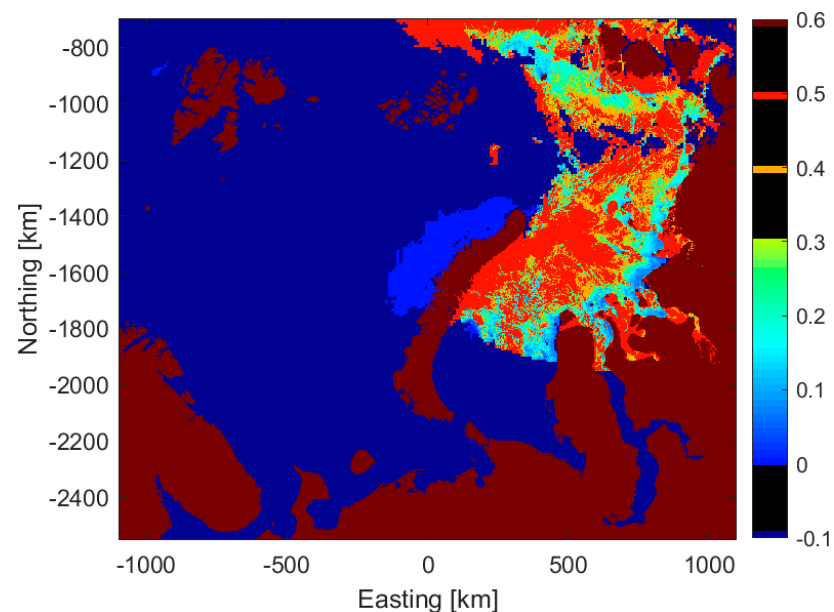


Figure 2. MODIS daily median ice thickness chart on 2 December 2015. Vertical bar shows the numerical scale for different sea ice thickness values and masks: 0.0–0.3 m for thin ice thickness, thickness range from 0.31–0.5 m with the value of 0.4 and >0.51 m with 0.5 m, and land and no-data masks with 0.6 m and -0.1 m, respectively. Pixel size is 1 km.

2.2. AMSR2 Radiometer Data

AMSR2 level L1R (resampled L1) T_B data [23] and L2 SIC swath data [37] were collected for four winters in October–May 2013–2017. Here, we use 36.5 and 89 GHz T_B data at the footprint size of the 36.5 GHz data ($7 \text{ km} \times 12 \text{ km}$) and 10.65 and 36.5 GHz T_B data at the 10.65 GHz footprint ($24 \text{ km} \times 42 \text{ km}$).

The L1R data at the 36.5 GHz (or 10.65 GHz) footprint over BKS were rectified to the PS coordinate system of the MODIS charts with 10 km (30 km for 10.65 GHz) grid size using linear interpolation. One 30 km pixel covers an area of 3×3 10 km pixels. The L2

SIC data were projected to a 10 km pixel size using nearest neighbor interpolation as it has a land mask. Using block averaging SIC data at 30 km grid size was then calculated. A daily SIC chart was calculated by temporal averaging of the SIC swath charts.

Over the Arctic Ocean one winter, October 2016–May 2017, L1R T_B and L2 SIC data were processed in a similar way as for the BKS. Here, the PS coordinate system of the SMOS h_i chart was used, see Section 2.7.

Land masks for the 10 and 30 km BSK grids were derived in [22]. Land masks for the Arctic T_B data at 10 and 30 km grids were obtained from the OSI SAF OSI-403-d global sea ice type product with 10 km grid [38].

2.3. FY-3C MWRI Radiometer Data

FY-3C is one of China's second-generation polar-orbiting meteorological satellites. It has an MWRI radiometer, which is a conical scanning imager at five frequencies (10.65, 18.7, 23.8, 36.5, and 89 GHz) with H- and V-polarization (10 channels in total) [39]. The footprints of the MWRI are larger than those for AMSR2: 51 km × 85 km at 10.65 GHz, 18 km × 30 km at 36.5 GHz, and 9 km × 15 km at 89 GHz. The swath width is 1400 km, slightly narrower than for AMSR2 (1450 km). MWRI has an incidence angle of around 53° whereas AMSR2 has 55°.

Here, we use FY-3C MWRI L2 CRM (Channels Resolution Match) T_B and L2 SIC products available at the FENGYUN Satellite Data Centre. MWRI data were downloaded for October 2014–April 2015 and for two winters in October–May 2015–2017. The MWRI CRM T_B data are not available for the January–April 2014 period of the MODIS swath h_{iM} charts. The 36.5 and 89 GHz T_B data used here are those sampled in the product to the footprint size of the 36.5 GHz data, 18 km × 30 km. This T_B data and SIC data were projected with 20 km pixel size using linear interpolation. The T_B data are used to calculate PR36 and GR8936H. Daily SIC data are calculated from the gridded SIC swath charts. GR3610H is calculated from the T_B data sampled to the footprint of the 10.65 GHz data, 51 km × 85 km. These T_B data are gridded to the PS projections with 40 km pixel size. A pixel in the 40-km grid covers a 2 by 2 block of 20 km pixels. Landmasks with 20 and 40 km pixel sizes were processed from the AMSR2 10 km landmask.

2.4. ERA5 Data

Atmospheric data for the T_B atmospheric corrections were extracted from the ECMWF's ERA5 reanalysis data [40,41]. The data extracted have a one-hour time step and 0.25° by 0.25° grid as well as the following parameters: 10-m wind speed (V_{10}), 2-m T_a , total column liquid water (LW), total column water vapor (WV), and skin temperature (T_S). The ERA5 data were sampled to the 10 (AMSR2) and 20 km (MWRI) PS grids with cubic interpolation and then block averaged for the 20 (AMSR2) and 40 km (MWRI) grids. The gridded data were further interpolated to the time stamps of the swath T_B datasets.

2.5. Combination of T_B and T_S Data

The datasets of the AMSR2 T_B for BKS (10 and 30 km grids) in conjunction with T_S data spanning three winter seasons from 2014 to 2017 are utilized to examine the average dependence of PR36, GR8936H, and GR8910H sea ice signatures on T_S as outlined in [13,22]. The following criteria were applied in this analysis: $SIC \geq 70\%$ and $T_S \leq -5$ °C. Similarly, T_B datasets from MWRI for BKS on 20 and 40 km grids and T_S data were combined. The size of the datasets used in these investigations ranges significantly from 2.0×10^6 to 40.8×10^6 samples.

2.6. Combination of T_B and MODIS Ice Thickness Data

Datasets from co-located MODIS swath h_{iM} and AMSR2 swath T_B , T_S , and T_a with pixel resolutions of 10 km and 30 km were integrated for the formulation of ATIDA2 as described in [13,22]. The thickness threshold for distinguishing between thin and thick ice is maintained at 20 cm. Specifically, combined T_B and pixel-based mean h_{iM} (\bar{h}_{iM}) data were

only chosen over AMSR2 pixels having relatively uniform h_{iM} and $SIC \geq 70\%$. Within the 10 km (30 km) data compilation, the total count of samples reached 101,054 (10,572). The sample count for thin ice ($\bar{h}_{iM} \leq 0.2$ m) is 21,241 and 1810 for the 10 and 30 km datasets. For a thick ice class of $0.2 < \bar{h}_{iM} < 1.0$ m (thick1 class), the number of samples is 18,148 (10 km) or 3578 (30 km). For the third class, thick ice $\bar{h}_{iM} \geq 1$ m (thick2 class) and there are 61,665 (10 km) or 5184 (30 km) samples. Approximately 94% of the thick1 samples were retrieved when $T_a < -20$ °C, whereas this figure is 57% for thin ice. In the thick2 class, the upper T_a limit was set to -25 °C as in warmer conditions, the h_{iM} retrieval may fail for ice thinner than 1 m as well [34].

In similar way, MODIS-MWRI datasets were compiled for the development of MTIDA2. The sample sizes are reduced in this case due to the larger pixel dimensions and the absence of T_B CRM data for the period from January to April 2014. The aggregate sample count for the 20 km (40 km) dataset stands at 27,406 (5517). For thin ice, the sample figures are 4996 and 807 for the 20 km and 40 km datasets, respectively. In the thick1 category, the sample sizes are 9189 (20 km) and 1822 (40 km), and for the thick2 category, there are 13,221 (20 km) and 2888 (40 km) samples. About 87% of the thick1 class samples are for $T_a < -20$ °C. This figure is 53% for thin ice.

2.7. SMOS Ice Thickness Data

The Alfred Wegener Institute, Helmholtz Centre for Polar and Marine Research, produces a daily sea ice thickness (h_{iS}) chart from the SMOS satellite data, which serves here as a guideline for assessing the accuracy of the Arctic ATIDA2 and MTIDA2 ice charts. The evaluation spans from October 2016 through to April 2017. Comprehensive information on the methodology for deriving the SMOS h_{iS} chart and its characteristics is documented in [2,4,42,43]. An evaluation study conducted in the Barents Sea indicated that the h_{iS} values tend to underestimate the actual ice thickness by approximately 50–60% on average [2]. This underestimation is not taken into account here in the data analyses.

The correlation coefficient against the validation datasets was 0.75 and the root mean square deviation (RMSD) was 0.31 m. Capability to retrieve h_{iS} is constrained by the sea ice temperature and salinity, with a maximum detectable thickness of up to 1.5 m [2]. It is recommended that the analysis of h_{iS} always incorporates considerations of its saturation ratio (the ratio of the retrieved to the maximum retrievable h_{iS}) and/or uncertainty [43]. Data characterized by a saturation ratio exceeding 95% or an uncertainty greater than 1 m are deemed unsuitable for use.

The daily h_{iS} chart has a 12.5 km pixel size and a daily gridded T_B , utilized for determining h_{iS} , which is derived from near-nadir T_{Bs} with an approximate footprint of 35–40 km [2]. This chart is produced in the PS grid of the National Snow and Ice Data Center (NSIDC) with a standard latitude of 70°N [44]. The latest version of the h_{iS} chart is v3.3, covering the Arctic Ocean from latitudes 50°N to 85°N, and available from 15 October to 15 April annually. The h_{iS} data were adapted to the AMSR2 10 km grid through nearest-neighbor interpolation and the AMSR2 10 km land mask was applied to this interpolated dataset.

3. Methods

The following methods used in this study are described. Most of the methods originate from our earlier studies in [13,22] and, therefore, they are described here only shortly.

3.1. Atmospheric Correction

The T_B data are corrected for the atmospheric effects due to WV , LW , V_{10} (wind roughened ocean surface), and T_S following the OSI SAF atmospheric correction method [24,26]. The OSI SAF correction method calculates a correction term ΔT_{Bc} as a difference between two T_B calculations with a parametrized RTM (radiative transfer model) described in [45,46]: T_{Bnwp} , T_B calculated with NWP (numerical weather prediction) data uses atmospheric data (T_S , V_{10} , WV , and LW), while T_{Bref} has an atmospheric reference state with zero V_{10} , WV ,

and LW and the same T_S as in T_{Bnwp} . ΔT_{Bc} is an estimate of the atmospheric contribution in the T_B measurement. Until recently, T_B data were not corrected for the influence of LW because its NWP model data were not accurate enough [24,25,47]. In the current version of the OSI SAF Global Sea Ice Concentration climate data record (product OSI-450-a) released in 2022, the correction for LW is now included. It was found that ERA5 has some skills representing LW variation in the Arctic and including LW in the T_B correction decreased the uncertainty of the retrieved SIC at low SIC values. In our earlier study in [13], the LW correction was not applied.

The corrected T_B is calculated as [24,26]

$$T_{Bc} = T_B - (T_{Bnwp} - T_{Bref}), \quad (1)$$

$$T_{Bnwp} = T_B(f, p, \theta_0, e_{si}, V_{10}, WV, LW, T_S, SIC), \quad (2)$$

$$T_{Bref} = T_B(f, p, \theta_0, e_{si}, 0, 0, 0, T_S, SIC), \quad (3)$$

where f is frequency, p is polarization, θ_0 is incidence angle, and e_{si} is sea ice emissivity. For e_{si} OSI SAF uses fixed emissivities (see Table 1), which are more accurate for FYI when compared to monthly FYI and multiyear ice (MYI) emissivities in [48]. Previously, in [13], ERA5 T_a instead of T_S was used in the atmospheric correction. Below, FYI and MYI emissivities (e_{FYI} and e_{MYI}) and FYI and MYI sea ice effective temperatures (T_{eff}^{FYI} and T_{eff}^{MYI}) by Mathew et al. [48] are denoted simply by ‘Mathew’.

Table 1. OSI SAF mixing coefficients for calculating T_{eff} with (4) and sea ice emissivities at different AMSR2 channels [46].

Parameter	Radiometer Channel									
	6.9V	6.9H	10.65V	10.65H	18.7V	18.7H	36.5V	36.5H	89V	89H
emissivity	0.96	0.88	0.9	0.9	0.95	0.90	0.93	0.88	0.90	0.83
T_{mix}	0.45	0.40	0.4	0.4	0.75	0.47	0.95	0.70	0.97	0.97

In [13], the T_B correction was modified to use wintertime mean Mathew e_{FYI} and e_{MYI} and Mathew T_{eff}^{FYI} and T_{eff}^{MYI} for T_{Bnwp} as well as T_{eff} reference values for T_{Bref} . Earlier, the winter time e_{FYI} and e_{MYI} were means of their wintertime monthly values (November to April) given in [48]. The reference T_{eff}^{FYI} and T_{eff}^{MYI} were calculated from average T_a s for three winter seasons. This modification was targeted to compensate the effect of spatial and temporal variation in T_{eff} on the measured T_B data. However, this reference T_a value may be too small for MIZ and also too small during freeze-up season, giving too large T_B corrections. Therefore, we switch to using a daily reference T_S (T_{Sref}) chart calculated by averaging the ERA5 hourly data within two days of previous and current dates. Furthermore, monthly Mathew e_{FYI} s and e_{MYI} s are interpolated to the daily scale with 15 days of moving averaging. Finally, OSI SAF T_{eff}^{FYI} is now used instead of the Mathew one. The OSI SAF T_{eff} s depend on both on T_S and ice bottom freezing temperature whereas Mathew T_{eff} s are the only function of T_S and thus, the OSI SAF T_{eff} s should be better for FYI.

In the following, the OSI SAF and Mathew et al. [48] sea ice data and interim stages needed to apply the atmospheric correction with the FYI and MYI data are presented.

3.1.1. OSI SAF Sea Ice Data

T_{eff} is calculated as a linear mixture between the sea ice bottom freezing temperature of 272 K and the sea ice surface temperature (T_{ssi} ; taken here as ERA5 T_S) [25,46]:

$$T_{eff} = T_{mix} \cdot T_{ssi} + (1 - T_{mix}) \cdot 272. \quad (4)$$

If the resulting $T_{eff} > 272$ K then T_{eff} is set to 272 K, i.e., the ice surface is under melting conditions. The mixing coefficient T_{mix} at each AMSR2 channel is shown in Table 1. At lower frequencies T_{eff} is higher, i.e., closer to 272 K, than at higher ones under cold conditions. Table 1 also shows the fixed e_{si} used in the default OSI SAF atmospheric correction.

3.1.2. Sea Ice Data by Mathew et al. [48]

The monthly e_{FYI} and e_{MYI} given in [48] are interpolated to the daily scale with 15 days moving averaging. Mathew et al. [48] derived linear relationships between T_{eff}^{FYI} and T_{eff}^{MYI} and the lowest level air temperature (T_{al}) in the Celsius scale at each AMSR-E frequency and independent of polarization. These linear relationships are of the following form [48]:

$$T_{eff} = a \cdot T_{al} + b. \quad (5)$$

There are different relationships for the winter months from December to March and for the spring (April–May) and freeze-up seasons (August to November). Here, T_{al} is approximated with the ERA5 T_S .

The change in T_{eff} s between the seasons is mitigated by weighted averages when the date is at maximum two days from the ending of a current or the beginning of a new season, i.e., from 28 November to 3 December or from 29 March to 3 April. The weighting factors are $[1:+1:6]/7$ and $[6:-1:1]/7$.

Figure 3 shows Mathew T_{eff} 's at 36.5 and 89 GHz for the winter months together with the OSI SAF T_{eff} s. The Mathew T_{eff} s increase slower with increasing T_S than the OSI SAF T_{eff} s and thus, their differences are not constant. The OSI SAF T_{eff} s saturate toward the freezing temperature of sea ice (272 K) with increasing T_S but Mathew T_{eff} s do not.

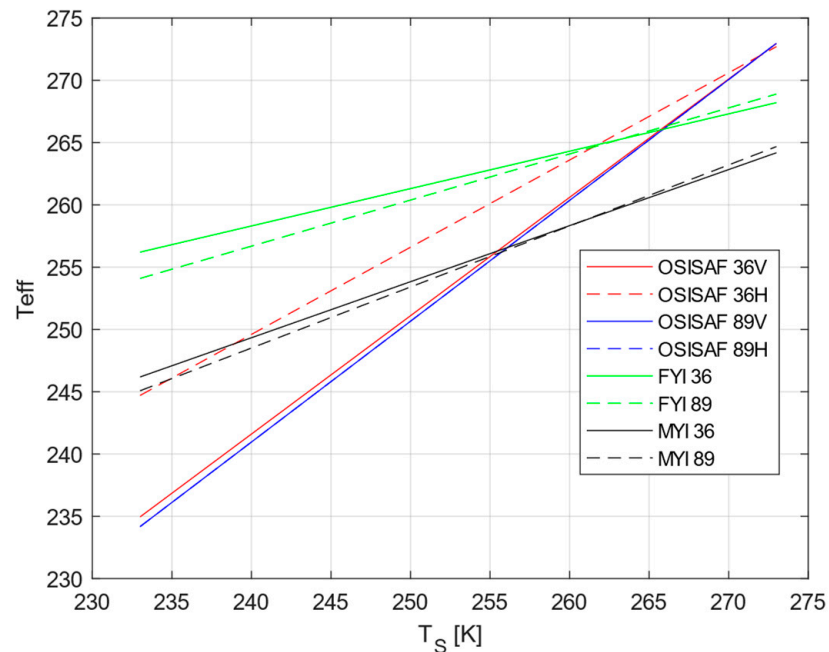


Figure 3. Sea ice effective temperatures at 36.5 and 89 GHz with the OSI SAF equation in (4) and for FYI and MYI for the winter months (December to March) by Mathew et al. [48]. The OSI SAF 89V and 89H T_{eff} s are the same.

3.1.3. Daily Surface Temperature Chart

Using two-day time interval (previous and current date), an average T_S chart is calculated from the hourly ERA5 T_S data at the 10/20 km grid. This average T_S chart is used for T_{eff} s in T_{Bref} . The daily T_S chart at the 30/40 km pixel size is obtained with block averaging the 10/20 km chart.

3.1.4. FYI and MYI Fractions

The use of separate FYI and MYI emissivities and T_{effs} in the T_B correction requires estimation of FYI and MYI fractions for each pixel. These are calculated from the NASA Team (NT) algorithm [49] SIC_{FYI} and SIC_{MYI} as

$$f_{FYI} = \frac{SIC_{FYI}}{SIC_{FYI} + SIC_{MYI}} \text{ and } f_{MYI} = \frac{SIC_{MYI}}{SIC_{FYI} + SIC_{MYI}}. \quad (6)$$

f_{FYI} and f_{MYI} are constrained from 0 to 1 range and their sum is always one. Unfortunately, f_{FYI} and f_{MYI} are quite noisy for a single swath and therefore, two days averaging of swath f_{FYI} and f_{MYI} is conducted and then rounded to 0.05 resolution (their sum is again one).

The NT SIC is based on the 18.7 and 36.5 GHz T_B data, which are in either the 30 km (AMSR2) or 40 km (MWRI) grid here. For calculating the 10 km (AMSR2) or 20 km (MWRI) grid, f_{FYI} and f_{MYI} of the 30/40 km grid T_B s are upscaled to the 10/20 km pixel size by replicating, e.g., a 30 km pixel contains 3×3 10 km T_B s of equal value. Following a SIC study by Shi et al. [50], the MWRI T_B data are matched to the SSMIS (Special Sensor Microwave Imager/Sounder) F17 data and then the SSMIS NT tie points are used. The T_B data matching is conducted using monthly linear regression equations.

Over BKS pixels with f_{MYI} are only allowed to occur within a MYI mask processed from the Arctic and Antarctic Research Institute (AARI), Russia, weekly ice charts [51] for October–May in 2014–2017 (three winter seasons). The polygonal AARI charts were gridded to 1 km pixel size and pixels that have at least one ‘old ice’ type (same as MYI) assignment were identified, resulting in a MYI mask. Next, this mask was processed at a 10 km pixel size by allowing a 10 km pixel to have MYI if at least one 1 km pixel within it had MYI. Finally, the MYI mask was smoothed by manual editing and also aggregated to 30 km pixel size (MYI is allowed if it least one 10 km pixel had MYI). This MYI mask allows f_{MYI} to occur only in the northern part of BKS. Previously, in [13], the MYI mask was not used.

The Arctic MYI mask was derived from the daily OSI SAF OSI-403-d global sea ice type product [38]. During a time period from 1 October 2016 to 31 May 2017, daily occurrences of MYI in each pixel was counted and from the resulting summary chart, the maximum extent of MYI was manually determined.

For the MWRI 20 and 40 km grids over BKS and Arctic MYI masks were processed from the AMSR2 10 km MYI masks.

3.1.5. Atmospheric Correction with FYI and MYI Data

Daily e_{si} charts are used for both T_{Bnwp} and T_{Bref} . Mathew e_{FYI} and e_{MYI} are combined into general e_{si} as

$$e_{si} = f_{FYI} \cdot e_{FYI} + f_{MYI} \cdot e_{MYI}. \quad (7)$$

Spatial variation is smoothed with 3×3 sliding window averaging. T_{Bref} has a bottom-of-atmosphere (BOA) T_B term (T_B^{BOA}), which is calculated as

$$T_B^{BOA} = f_{FYI} \cdot e_{FYI} \cdot T_{eff}^{FYI} + f_{MYI} \cdot e_{MYI} \cdot T_{eff}^{MYI}, \quad (8)$$

where e_{FYI} and e_{MYI} are daily values and T_{eff}^{FYI} and T_{eff}^{MYI} are calculated using the daily T_S chart. Like for e_{si} with (7) spatial variation is smoothed with 3×3 sliding window averaging.

Swath T_B^{BOA} for T_{Bnwp} is calculated as (8), the same daily e_{FYI} , e_{MYI} , f_{FYI} , and f_{MYI} are used, but T_{eff}^{FYI} and T_{eff}^{MYI} are now with instantaneous T_S (ERA5 T_S interpolated to the time of the T_B swath acquisition). Sliding window averaging is also applied here.

3.2. Thin Ice Detection with AMSR2 or MWRI T_B Data

Previously, we introduced a new iterative algorithm for detecting thin ice using the AMSR2 T_B data, denoted as ATIDA2 [13]. This algorithm employs linear discriminant

analysis (LDA) to categorize PR36 and GR8936H signatures, alongside a method for correcting misidentifications of thin ice, referred to as thick ice restoration using GR3610H. This correction technique effectively eliminates inaccuracies in the thin ice detection due to overlapping PR36 and GR8936H signatures. ATIDA2 is applied only when $T_a \leq -5$ °C and SIC $\geq 70\%$ to minimize misclassification of thick ice as thin ice. In this study, ATIDA2 is re-determined for the AMSR2 T_B data with the new atmospheric correction method and a similar algorithm is also determined for the first time for the MWRI T_B data, denoted as MTIDA2.

The determination of the LDA classifier of ATIDA2 is described in detail [13] and the following are some main points of its determination process. (a) During the learning phase, we use samples from the thin and thick1 classes where T_a is below -20 °C and set a threshold for thin ice at PR36 < 0.06 . Eliminating higher PR36 values brings the PR36–GR8936H distribution closer to a Gaussian distribution, making it better suitable for the LDA classification. The thick2 class is omitted to prevent its overwhelming influence on the combined covariance matrix, given its clear distinction from the thin ice class. (b) Samples from the thin ice and thick1 classes are randomly split into equal-sized training and testing datasets. The thick2 class, along with thin ice samples having $T_a \geq -20$ °C or PR36 > 0.06 , and all thick1 with $T_a \geq -20$ °C are included in the testing dataset. (c) In the training and testing datasets, the GR8936H and PR36 signatures are normalized to T_S of -25 °C. (d) Due to the random nature of the training dataset, the division to training and testing datasets and determination of the LDA classifier is repeated 1000 times and average LDA coefficients are calculated. This extensive sampling ensures that the derived LDA coefficients remain consistent in repeated experiments.

The LDA classifier accuracy is measured through specific probabilities: the incorrect labeling of the thick1 category as thin ice (type Ia error), the misidentification of the thick2 category as thin ice (type Ib error), and the erroneous classification of thin ice as thick ice (type II error). In the process of integrating the AMSR2/MWRI thin ice chart with the SAR data for categorizing sea ice, we prefer to minimize the type I errors. Our goal for the type Ia error is about 10%. To obtain this error level involves manual adjustments of the LDA threshold (th) in increments of 0.05. That is, with the selected threshold, the type Ia error I is around 10% (type Ib is already minimal at $th = 0$). Generally, elevating the threshold reduces the occurrence of the type Ia and Ib errors but leads to an increase in the type II error.

The form of the LDA classifier determined in [13] was

$$LDA_s = 44.1 \cdot PR36 + 21.4 \cdot GR8936H - 0.8, \quad (9)$$

$$\text{thin ice if } LDA_s > 0.6, \quad (10)$$

where LDA_s is the LDA score value.

The study [13] identified instances where a significant thick ice area was misclassified as thin ice on the subsequent day. This misclassification is attributed to modifications in the sea ice or snow characteristics that blur the distinctions between thin and thick ice signatures. To address this issue, the restoration of thick ice was explored through the employment of various V- and H-polarized GR's across the frequency spectrum of 10.65 to 89 GHz. The GR that most effectively reduced the type I error was identified as GR3610H. The GR3610H threshold (th_{GR}) is adjusted with a 0.005 step to give very small the type II error, just below 10%, i.e., $GR3610H < th_{GR}$ includes mostly thick ice signatures. The learning data herein encompassed all the thick1 and thin data normalized to T_S of -25 °C; the testing data are the entire dataset, also normalized to -25 °C. In [13], we applied thick ice restoration with

$$GR3610H \leq 0.005. \quad (11)$$

In ATIDA2 (MTIDA2), the thin vs. thick ice labeling is first carried out with (10) at 10 km (20 km in MTIDA2) resolution. Then, the thick ice restoration procedure (11) is performed at 30 km (40 km) pixel size.

The swath ATIDA2/MTIDA2 charts are incorporated into a single more dependable daily thin ice chart, as detailed in [13,22]. The swath and daily charts have the same pixel size (10/20 km). For the purpose of labeling a pixel as thin ice, it is a requisite that over 50% of the daily detections are categorized as such. The daily chart categorizes SIC into five WMO SIC categories [36]: $SIC \leq 10\%$, $10 < SIC \leq 40\%$, $40 < SIC < 70\%$, $70 \leq SIC \leq 90\%$, and $SIC > 90\%$ and identifying thin ice versus thick ice within the last two categories. Pixels that consistently receive unknown ice type assignments ($T_a > -5^\circ\text{C}$) throughout the entire day are labeled accordingly in the chart.

4. Results

Below the ATIDA2 and MTIDA2 thin ice detection algorithms are described, followed by statistical comparison between the Arctic ATIDA2 and MTIDA2 charts, and finally, comparison of the charts to the SMOS ice thickness chart.

4.1. Thin Ice Detection—ATIDA2 for AMSR2

ATIDA2 is an iterative algorithm that initiates with the detection of thin ice using LDA, which is subsequently followed by a process for restoring thick ice. As previously established in [13], GR3610H acts as the optimal GR within the 10.65 to 89 GHz frequency spectrum for the thick ice restoration. The procedure for detecting thin ice is performed at 10 km pixel size, then a coarser pixel size, 30 km, is used for the thick ice restoration phase. Prior to the execution of ATIDA2, the quantities PR36, GR8936H, and GR3610H are adjusted to fixed T_S set at -25°C . Following [13,22], the average relationships between the PR and GR signatures and T_S were established via linear regressions. These regressions analyzed the mean signatures inside 2°C wide T_S intervals with bin centers spanning from -34°C to -6°C .

The re-determined ATIDA2 for the Arctic is the following:

1. Atmospheric correction of the T_B data. OSI SAF correction with FYI and MYI data: pixel emissivity is a mixture of Mathew e_{FYI} and e_{MYI} according to daily FYI and MYI fractions from the NT SIC data. The MYI fraction is only allowed within a MYI mask. OSISAF T_{eff}^{FYI} and Mathew T_{eff}^{MYI} with the daily T_{Sref} chart used;
2. Thin ice detection with PR36 and GR8936H

$$LDA_s = 52.5 \cdot PR36 + 25.3 \cdot GR8936H - 1.0, \quad (12)$$

$$\text{thin ice if } LDA_s > 0.6. \quad (13)$$

3. T_S scaling of PR36 and GR8936H is conducted with

$$PR36 = 0.0009 \cdot T_S + 0.053, \quad (14)$$

$$GR8936H = 0.0015 \cdot T_S - 0.006. \quad (15)$$

4. Thick ice restoration with

$$GR3610H \leq 0.005. \quad (16)$$

T_S scaling of GR3610H is conducted with:

$$GR3610H = 0.0010 \cdot T_S + 0.023. \quad (17)$$

Figure 4 illustrates examples of the ATIDA2 Arctic ice charts. On average, 16% of the pixels within a single swath dataset were identified as thin ice with the LDA_s classifier, and of these, an average of 53% were restored as thick ice using GR3610H. The percentage of thin ice pixels restored as thick ice within individual swaths varied a lot, from 0% to 100%, and STD was 20%.

The performance of the LDA classifier, when evaluated using the testing data part of the combined AMSR2-MODIS dataset, gave the following accuracy metrics: a type Ia error of

9.6%, a type Ib error of 0.7%, and a type II error of 30.2%. For comparison, the LDA classifier was also trained with the original uncorrected T_B data. The errors are now slightly larger, i.e., 9.8%, 0.9%, and 31.3%. This demonstrates a contribution of the T_B atmospheric correction.

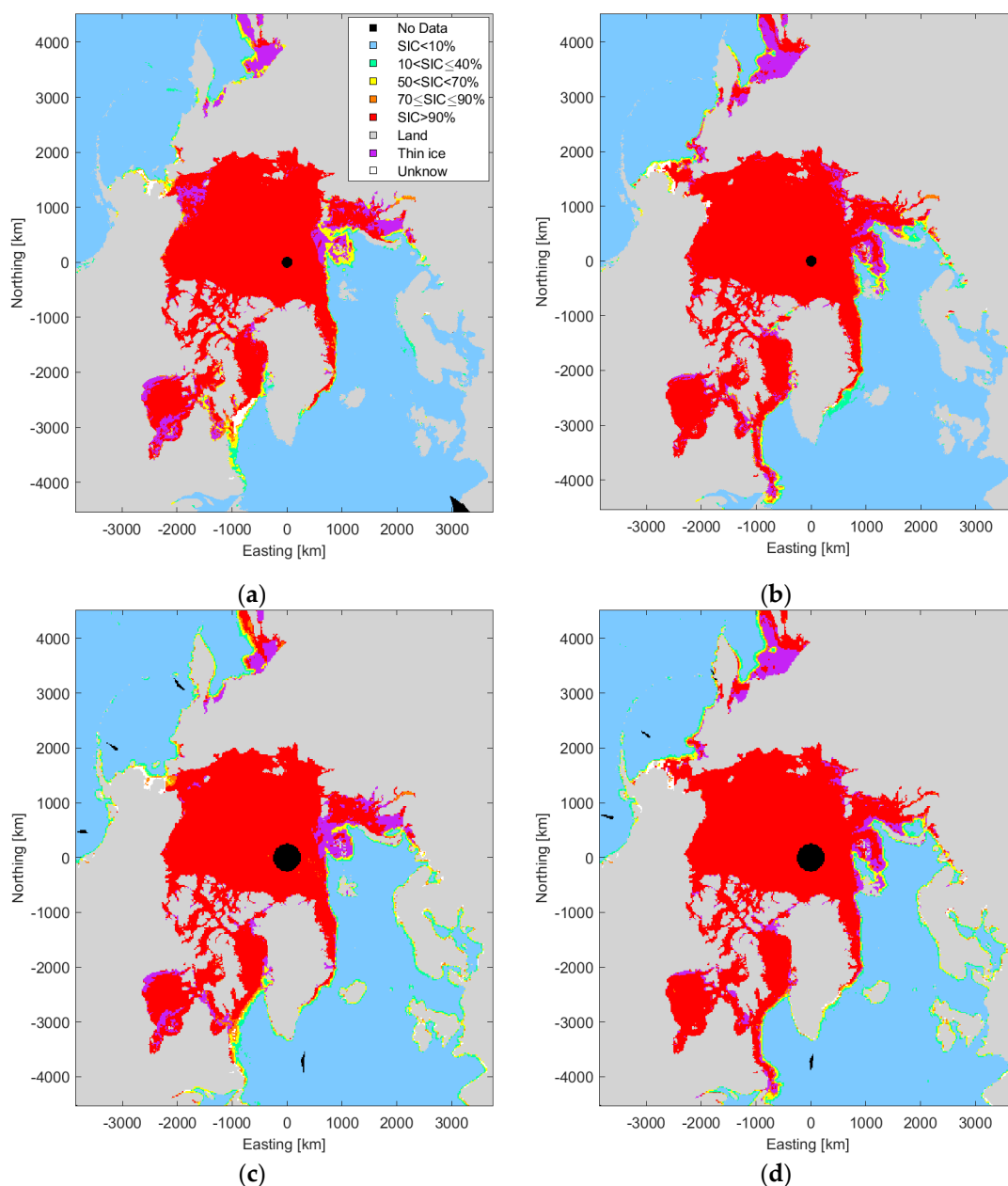


Figure 4. AMSR2 and MWRI daily thin ice charts over the Arctic; AMSR2 daily thin ice chart on (a) 31 December 2016 and (b) 31 January 2017; and MWRI daily thin ice chart on (c) 31 December 2016 and (d) 31 January 2017.

The accuracy of the ATIDA2 daily ice chart was assessed using the MODIS daily h_{iM} charts for two winter seasons spanning 2015–2017 (November–April). This assessment categorized sea ice in the MODIS charts into thin and thick classes at a 10 km pixel resolution, as detailed in [13]. The evaluation involved counting the number of MODIS h_{iM} pixels containing ice thickness data within each AMSR2 pixel (up to a maximum of 100 pixels). A label of thick (or thin) ice was set if at least 90% of the h_{iM} pixels had estimates greater than 20 cm (or $h_{iM} \leq 20$ cm), respectively. The type I and II errors, when compared against two seasons of the MODIS h_{iM} charts, were found to be 7.0% and 41.9%,

respectively. In [13], these errors were reported as 8.7% and 37.0%. Therefore, there was a slight improvement in the type I error, which is considered more significant than the deterioration observed in the type II error. The error figures with the daily h_{iM} charts are somewhat unreliable as the cloud masking in the chart did not include manual editing.

In the analysis of how T_a affects the type I and II errors, it was observed that the probability density functions (pdfs) of daily mean air temperature (T_{am}) associated with these errors exhibit almost symmetric distributions. Moreover, type II errors are more prevalent under extremely cold conditions: the proportion of T_{am} falling below $-20\text{ }^\circ\text{C}$ stands at 0.52 for type II errors, whereas for type I errors, this proportion is just 0.12. The lack of correlation between the errors and T_{am} indicates that the T_S scaling of PR and GR signatures work properly. In the daily ice charts, pixels labeled as thick ice predominantly coincide with daily SIC $> 90\%$ (accounting for 90% of such pixels), whereas around 70% of pixels with the thin ice label have SIC values ranging from 70 to 90%. This follows SIC underestimation for thin ice [25,27–29].

4.2. Thin Ice Detection—MTIDA2 for MWRI

For determination of MTIDA2, there are coincident MWRI CRM T_B data and MODIS h_{iM} charts only for the time period October 2014–April 2015. The resulting MTIDA2 for the Arctic is

1. Same atmospheric correction as for the AMSR2 T_B data;
2. Thin ice detection with PR36 and GR8936H

$$LDA_s = 63.3 \cdot PR36 + 36.2 \cdot GR8936H - 1.5 \quad (18)$$

$$\text{thin ice if } LDA_s > 0.8. \quad (19)$$

T_S scaling of PR36 and GR8936H is conducted with:

$$PR36 = 0.0011 \cdot T_S + 0.057, \quad (20)$$

$$GR8936H = 0.0019 \cdot T_S - 0.008. \quad (21)$$

3. Thick ice restoration with

$$GR3610H \leq 0.005. \quad (22)$$

T_S scaling of GR3610H is conducted with

$$GR3610H = 0.0017 \cdot T_S + 0.044. \quad (23)$$

Samples of the MTIDA2 Arctic daily charts are depicted in Figure 4. The accuracy of MTIDA2 determined with the testing data part of the combined MWRI-MODIS dataset is the following: type Ia error is 10.7%, type Ib 0.2%, and type II 36.0%. The type Ia and II errors are slightly larger than those for ATIDA2 (9.6% and 30.2%). The ATIDA2 vs. MTIDA2 accuracy differences are likely due to larger footprints of MWRI, which leads to larger spatial averaging of T_B signatures and thus, less detection of thin ice. In addition, the MWRI-MODIS data are missing the January–April 2014 period.

The type I and II errors relative to the MODIS daily ice charts, categorized into thin and thick ice at the 20 km pixel resolution of the MTIDA2 chart, are at 4.4% and 53.2%, respectively. The type I error for the MTIDA2 chart is smaller compared to that of the ATIDA2 chart (7.0%) but the type II error for MTIDA2 exceeds that of ATIDA2 (41.9%). It is again noted, however, that the accuracy metrics derived from the MODIS daily charts are just estimations. The T_{am} pdfs for the type I and II errors display a near symmetrical distribution around their mean values, with type II errors being more frequent under very cold conditions: for the type II error, the proportion of $T_{am} < -20\text{ }^\circ\text{C}$ is 0.47, in contrast to only 0.12 for type I errors. In the MTIDA2 chart, the majority of thick ice pixels are found in regions where the daily SIC $> 90\%$ (91% of pixels), whereas 44% of thin ice pixels are associated with SIC ranging from 70 to 90%. For the ATIDA2 chart, the thin ice figure was

much higher, at 70%. The difference is due to different SIC algorithms used for the L2 AMSR2 and MWRI products.

4.3. Comparison of AMSR2 and MWRI Arctic Daily Thin Ice Charts

Here, ATIDA2 and MTIDA2 Arctic charts for October 2016–May 2017 are compared to each other. The first comparison is to investigate the statistics of the thick ice restoration in the Arctic swath charts. This is conducted using swath charts, which had at least 100 thin ice pixel detections in an ATIDA2 chart (10 km pixel) and 25 detections in an MTIDA2 chart (20 km). The number of the ATIDA2 charts is 3457 and that of the MTIDA2 charts is 3286. The ATIDA2 and MTIDA2 swath charts cannot be directly compared to each other as the acquisition times are different. The mean thick ice restoration fraction, thick ice restoration pixels/thin ice pixels, is 0.53 for ATIDA2 and 0.44 for MTIDA2. The 90th percentile is larger for ATIDA2, 0.80, than, for MTIDA2, 0.73. Thus, thick ice restoration happens more often in ATIDA2 and this is due to different resolutions.

Further comparison is conducted using the daily charts. For this, the MTIDA2 20 km charts are replicated to 10 km pixel size. Pixels from both charts which show either thin class or SIC classes 70–90% and >90% (both represent thick ice) are used in the comparison, i.e., in a total of three classes, the results are shown as a confusion matrix in Table 2.

Table 2. Confusion matrix between ATIDA2 and MTIDA2 daily Arctic thin ice chart classes: thick ice with SIC 70–90% or SIC > 90% and thin ice. Calculated pixel-wise and ATIDA2 as ‘ground truth’.

AMSR2	MWRI		
	Thick, 70–90%	Thick, >90%	Thin Ice
thick, 70–90%	21%	57%	22%
thick, >90%	1%	98%	1%
thin ice	7%	40%	53%

For the thick ice with SIC > 90% the correspondence in the ATIDA2 and MTIDA2 charts is very high but for the thin ice class only it is 53% and for the thick ice with 70–90% SIC it is only 21%. Latter disagreement can be explained by different SIC data used; the MWRI SIC data have in general higher SIC values than the AMSR2 SIC. The thin ice disagreement is likely due to different resolutions, as a coarser resolution in the MTIDA2 chart leads to less detection of thin ice. For the MTIDA2 chart pixels with thin ice class, 72% of co-incident ATIDA2 pixels also show thin ice.

4.4. Comparison against SMOS Sea Ice Thickness Chart

To facilitate comparison with the ATIDA2 chart, the SMOS h_{iS} chart with a 12.5 km pixel size, was resampled to the 10 km grid using nearest neighbor interpolation. This resampled SMOS h_{iS} chart was then further block averaged into 20 km pixel size, aligning it for comparison with the MWRI2 chart. Subsequently, the daily SMOS h_{iS} data were labeled into thin and thick ice categories based on a thickness threshold of 0.2 m. Comparisons between the ATIDA2/MTIDA2 and SMOS charts were conducted on a daily basis, focusing on pixels with valid data in both datasets, from which mean type I and II errors were derived using the SMOS chart as a benchmark. Additionally, statistical analysis of the h_{iS} data within the ATIDA2/MTIDA2 defined thin and thick ice categories were performed. The h_{iS} data, collected daily from 15 October 2016 to 15 April 2017, included only h_{iS} data with a saturation ratio below 90% and uncertainty of less than 1 m [43]. The reliability of these accuracy evaluations against the SMOS chart is somewhat limited due to the high uncertainty of 0.31 m for h_{iS} [2], especially when considered in relation to the 0.2 m thickness threshold distinguishing thin ice and thick ice categories.

The mean type I and II errors identified for the ATIDA2 chart are 3.8% (with std of 2.1%) and 50.7% (std of 12.4%), respectively. When aggregating all daily h_{iS} data, the mean thickness for the thin ice category is 0.21 m (1.34×10^6 samples) and 0.51 m for the thick

ice category (5.45×10^6 samples). The proportion of $h_{iS} \leq 0.2$ m for the thin ice category is average, at 0.58, while for the thick ice category, the proportion of $h_{iS} > 0.2$ m is very high, at 0.86. Figure 5 shows the frequency distributions of h_{iS} data for the ATIDA2 chart's thin ice and thick ice categories. For the MTIDA2 chart, the mean type I and II errors are 2.7% (with std of 1.6%) and 59.0% (std of 12.1%), respectively. Notably, the type II error is considerable for both charts, which may be partially attributed to the inaccuracies within the SMOS dataset. For the thin ice category under the MTIDA2 chart, the mean h_{iS} is 0.18 m (0.27×10^6 samples) and for the thick ice category, the mean is 0.48 m (1.49×10^6 samples). These means closely resemble those for the ATIDA2 chart (0.21 m and 0.51 m). For the MTIDA2 thin ice category, the proportion of $h_{iS} \leq 0.2$ m is 0.67, i.e., better than for ATIDA2, and for the thick ice category, the proportion of $h_{iS} > 0.2$ m is high, at 0.81, as illustrated in Figure 6.

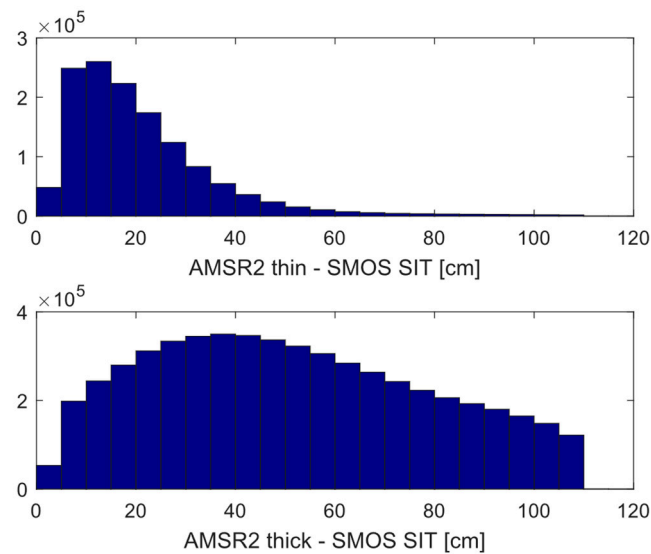


Figure 5. SMOS sea ice thickness distributions for the thin and thick ice classes in the AMSR2 Arctic thin ice chart. Bin width is 5 cm.

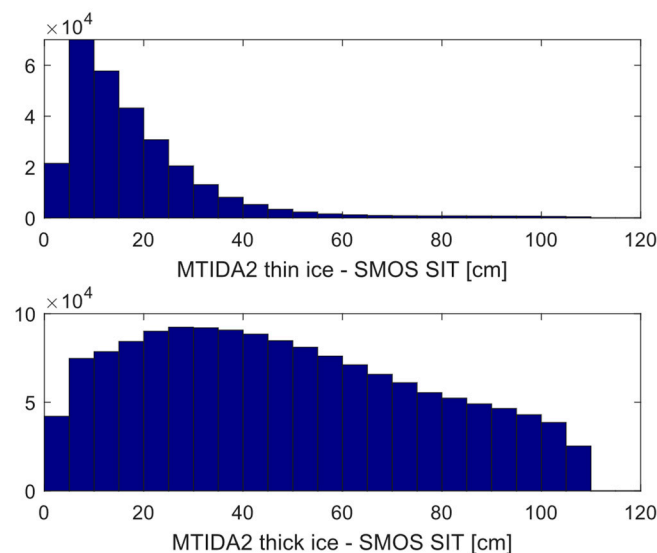


Figure 6. SMOS sea ice thickness distributions for the thin and thick ice classes in the MWRI Arctic thin ice chart. Bin width is 5 cm.

All three thickness charts contain their own uncertainties. Inspection of the frequency distributions shown in Figures 5 and 6 as well as the reasonable values of the means for the

ATIDA2 and MTIDA2 thick and thin ice categories in the SMOS data support the following conclusion. We can infer that both ATIDA2 and MTIDA2 charts have a rough match with the SMOS data in the thin ice vs. thick ice classification.

5. Discussion and Conclusions

The investigations herein extend our previous study [13], where an algorithm ATIDA2 for thin ice detection was presented. The same approach was applied to the FY-3C MWRI radiometer data resulting in the MTIDA2 thin ice identification algorithm. We also redefined the ATIDA2 algorithm for the AMSR2 data. This was needed as the T_B atmospheric correction was modified to better compensate for this temporal and spatial variation in sea ice T_{eff} . The results showed that thin ice detection with MWRI data, which has roughly two times coarser resolution than the AMSR2 data, is also possible with sufficient accuracy.

For both the AMSR2 and MWRI swath T_B data, LDA is utilized for the classification of PR36 and GR8936H signatures for thin ice detection, and GR3610H is applied for the restoration of falsely detected thin ice, mitigating errors due to thin ice and FYI or MYI signature mixing. The upper limit for thin ice thickness remained at 20 cm, consistent with [13]. The ATIDA2 algorithm generates a daily thin ice chart at a 10 km grid, whereas the MTIDA2 chart is produced at a 20 km grid. The daily charts are compiled from the swath charts with the same pixel sizes. Thin ice detection is performed only when $SIC \geq 70\%$ and $T_a < -5\text{ }^\circ\text{C}$, to limit the incorrect identification of thick ice as thin ice. The atmospheric correction of T_B data precedes the thin ice detection process and follows the OSI SAF atmospheric correction methodology [24,26].

Both ATIDA2 and MTIDA2 algorithms were trained and evaluated using the MODIS h_{iM} charts as reference. On average, the likelihood of misclassifying thick ice as thin ice in the ATIDA2 daily chart is 7.0% and 41.9% for reverse misclassification. Corresponding accuracy figures for the MTIDA2 daily charts are 4.5% and 52.4%. The higher type II error for MTIDA2 stems from the MWRI's coarser resolution, which results in larger spatial averaging of T_B signatures and, therefore, reduced thin ice detection.

A comparative analysis between the MTIDA2 and ATIDA2 charts showed a 98% match for the thick ice category with SIC above 90% but only 54% for the thin ice category and 21% for the thick ice category with SIC between 70–90%. The discrepancy in thin ice detection can be attributed to the MWRI's coarser resolution. When comparing the ATIDA2 chart against the MTIDA2 chart, the agreement rate for thin ice was 72%. A larger proportion of high SIC values in the MWRI SIC data contributes to the disagreement in the thick ice category with SIC 70–90%. The comparison of the ATIDA2 and MTIDA2 charts with the SMOS ice thickness chart indicated a general concurrence in the classification of thin versus thick ice.

Thin ice detection algorithms developed earlier for radiometer data were targeted to detect either polynyas [19,20] (polynya signature simulation method (PSSM)) or wide leads within pack ice [21]. Our ATIDA2/MTIDA2 can detect polynyas and very wide leads (~10 or 20 km in width) and also thin ice in MIZ where it may have a large coverage during the freeze-up season. Compared to PSSM, ATIDA2/MTIDA2 offers a simpler approach for polynya detection, facilitating its application to vast radiometer datasets. The successful detection of thin ice using AMSR2 and MWRI data suggests potential applicability to AMSR-E data, though SSM/I and SSMIS datasets are unsuitable due to the absence of the 10.65 GHz channel. Monitoring of ice thickness and thickness production rates in polynyas have been investigated in many studies, e.g., [5–12]. In these studies, algorithms were trained using h_i calculated based on T_S from TIR (thermal infrared) imagery. Estimation of h_i is mostly conducted up to 20 cm thickness. However, herein, estimation of thin ice h_i with sufficient accuracy is practically impossible due to the significant variability in the MODIS h_{iM} versus PR36 data. We reached this conclusion in [22] based on our extensive MODIS training dataset that included thin ice from polynyas, ice edges, and large MIZ areas during freeze-up.

The main uncertainties in the thin ice detection and thickness retrieval with any radiometer algorithm include T_B signature mixing from various surface types (open water, thin ice, FYI, and MYI), low SIC in thick ice that may resemble thin ice signatures at 100% SIC, and ice surface effects like snow cover on thicker thin ice (~10–30 cm) and roughness, which can generate signatures similar to those of thick ice [14,30–32]. We assume that further notable improvements in thin ice detection require additional satellite data, such as a combination of radiometer and scatterometer data, e.g., [52].

The AMSR2 and MWRI daily thin ice charts aim to complement SAR data for sea ice classification tasks. The ATIDA2 and MTIDA2 algorithms prioritize minimizing the mislabeling of thick ice as thin ice—a serious flaw for ship navigation. For snow depth and SIC algorithms, the charts can show the occurrence of thin ice either for corrective actions or pixel flagging.

Author Contributions: Conceptualization, M.M. and M.S.; methodology, M.M. and M.S.; software, M.M.; validation, M.M.; formal analysis, M.M.; data curation, M.M.; writing—original draft preparation, M.M.; writing—review and editing, M.M. and M.S.; project administration, M.M. All authors have read and agreed to the published version of the manuscript.

Funding: This research received no external funding.

Data Availability Statement: The raw data supporting the conclusions of this article will be made available by the authors on request.

Conflicts of Interest: The authors declare no conflicts of interest.

References

1. Kaleschke, L.; Tian-Kunze, X.; Maaß, N.; Mäkynen, M.; Drusch, M. Sea Ice Thickness Retrieval from SMOS Brightness Temperatures during the Arctic Freeze-up Period. *Geophys. Res. Lett.* **2012**, *39*, L05501. [[CrossRef](#)]
2. Kaleschke, L.; Tian-Kunze, X.; Maaß, N.; Beitsch, A.; Wernecke, A.; Miernecki, M.; Müller, G.; Fock, B.H.; Gierisch, A.M.U.; Schlünzen, K.H.; et al. SMOS Sea Ice Product: Operational Application and Validation in the Barents Sea Marginal Ice Zone. *Remote Sens. Environ.* **2016**, *180*, 264–273. [[CrossRef](#)]
3. Huntemann, M.; Heygster, G.; Kaleschke, L.; Krumpfen, T.; Mäkynen, M.; Drusch, M. Empirical Sea Ice Thickness Retrieval during the Freeze-up Period from SMOS High Incident Angle Observations. *Cryosphere* **2014**, *8*, 439–451. [[CrossRef](#)]
4. Tian-Kunze, X.; Kaleschke, L.; Maaß, N.; Mäkynen, M.; Serra, N.; Drusch, M.; Krumpfen, T. SMOS-Derived Thin Sea Ice Thickness: Algorithm Baseline, Product Specifications and Initial Verification. *Cryosphere* **2014**, *8*, 997–1018. [[CrossRef](#)]
5. Martin, S.; Drucker, R.; Kwok, R.; Holt, B. Estimation of the Thin Ice Thickness and Heat Flux for the Chukchi Sea Alaskan Coast Polynya from Special Sensor Microwave/Imager Data, 1990–2001. *J. Geophys. Res. Ocean.* **2004**, *109*, C10012. [[CrossRef](#)]
6. Tamura, T.; Ohshima, K.I.; Markus, T.; Cavalieri, D.J.; Nishashi, S.; Hirasawa, N. Estimation of Thin Ice Thickness and Detection of Fast Ice from SSM/I Data in the Antarctic Ocean. *J. Atmos. Ocean. Technol.* **2007**, *24*, 1757–1772. [[CrossRef](#)]
7. Tamura, T.; Ohshima, K.I. Mapping of Sea Ice Production in the Arctic Coastal Polynyas. *J. Geophys. Res. Ocean.* **2011**, *116*, C07030. [[CrossRef](#)]
8. Iwamoto, K.; Ohshima, K.I.; Tamura, T. Improved Mapping of Sea Ice Production in the Arctic Ocean Using AMSR-E Thin Ice Thickness Algorithm. *J. Geophys. Res. Ocean.* **2014**, *119*, 3574–3594. [[CrossRef](#)]
9. Ohshima, K.I.; Nishashi, S.; Iwamoto, K. Global View of Sea-Ice Production in Polynyas and Its Linkage to Dense/Bottom Water Formation. *Geosci. Lett.* **2016**, *3*, 13. [[CrossRef](#)]
10. Nakata, K.; Ohshima, K.I.; Nishashi, S. Estimation of Thin-Ice Thickness and Discrimination of Ice Type from AMSR-E Passive Microwave Data. *IEEE Trans. Geosci. Remote Sens.* **2019**, *57*, 263–276. [[CrossRef](#)]
11. Nakata, K.; Ohshima, K.I.; Nishashi, S. Mapping of Active Frazil for Antarctic Coastal Polynyas, with an Estimation of Sea-ice Production. *Geophys. Res. Lett.* **2021**, *48*, e2020GL091353. [[CrossRef](#)]
12. Nakata, K.; Ohshima, K.I. Mapping of Active Frazil and Sea Ice Production in the Northern Hemisphere, with Comparison to the Southern Hemisphere. *J. Geophys. Res. Ocean.* **2022**, *127*, e2022JC018553. [[CrossRef](#)]
13. Mäkynen, M.; Similä, M. AMSR2 Thin Ice Detection Algorithm for the Arctic Winter Conditions. *IEEE Trans. Geosci. Remote Sens.* **2022**, *60*, 1–18. [[CrossRef](#)]
14. Hwang, B.J.; Ehn, J.K.; Barber, D.G.; Galley, R.; Grenfell, T.C. Investigations of Newly Formed Sea Ice in the Cape Bathurst Polynya: 2. Microwave Emission. *J. Geophys. Res. Ocean.* **2007**, *112*, C05003. [[CrossRef](#)]
15. Naoki, K.; Ukita, J.; Nishio, F.; Nakayama, M.; Comiso, J.C.; Gasiewski, A. Thin Sea Ice Thickness as Inferred from Passive Microwave and in Situ Observations. *J. Geophys. Res. Ocean.* **2008**, *113*, C02S16. [[CrossRef](#)]

16. Ohshima, K.I.; Tamaru, N.; Kashiwase, H.; Nihashi, S.; Nakata, K.; Iwamoto, K. Estimation of Sea Ice Production in the Bering Sea from AMSR-E and AMSR2 Data, with Special Emphasis on the Anadyr Polynya. *J. Geophys. Res. Ocean.* **2020**, *125*, e2019JC016023. [[CrossRef](#)]
17. Nihashi, S.; Ohshima, K.I.; Tamura, T. Sea-Ice Production in Antarctic Coastal Polynyas Estimated from AMSR2 Data and Its Validation Using AMSR-E and SSM/I-SSMIS Data. *IEEE J. Sel. Top. Appl. Earth Observ. Remote Sens.* **2017**, *10*, 3912–3922. [[CrossRef](#)]
18. Kashiwase, H.; Ohshima, K.I.; Fukamachi, Y.; Nihashi, S.; Tamura, T. Evaluation of AMSR-E Thin Ice Thickness Algorithm from a Mooring-Based Observation: How Can the Satellite Observe a Sea Ice Field with Nonuniform Thickness Distribution? *J. Atmos. Ocean. Technol.* **2019**, *36*, 1623–1641. [[CrossRef](#)]
19. Markus, T.; Burns, B.A. A Method to Estimate Subpixel-Scale Coastal Polynyas with Satellite Passive Microwave Data. *J. Geophys. Res. Ocean.* **1995**, *100*, 4473–4487. [[CrossRef](#)]
20. Hunewinkel, T.; Markus, T.; Heygster, G.C. Improved Determination of the Sea Ice Edge with SSM/I Data for Small-Scale Analyses. *IEEE Trans. Geosci. Remote Sens.* **1998**, *36*, 1795–1808. [[CrossRef](#)]
21. Röhrs, J.; Kaleschke, L.; Bröhan, D.; Siligam, P.K. An Algorithm to Detect Sea Ice Leads by Using AMSR-E Passive Microwave Imagery. *Cryosphere* **2012**, *6*, 343–352. [[CrossRef](#)]
22. Mäkynen, M.; Similä, M. Thin Ice Detection in the Barents and Kara Seas Using AMSR2 High-Frequency Radiometer Data. *IEEE Trans. Geosci. Remote Sens.* **2019**, *57*, 7418–7437. [[CrossRef](#)]
23. Maeda, T.; Taniguchi, Y.; Imaoka, K. GCOM-W1 AMSR2 Level 1R Product: Dataset of Brightness Temperature Modified Using the Antenna Pattern Matching Technique. *IEEE Trans. Geosci. Remote Sens.* **2016**, *54*, 770–782. [[CrossRef](#)]
24. Andersen, S.; Tonboe, R.; Kern, S.; Schyberg, H. Improved Retrieval of Sea Ice Total Concentration from Spaceborne Passive Microwave Observations Using Numerical Weather Prediction Model Fields: An Intercomparison of Nine Algorithms. *Remote Sens. Environ.* **2006**, *104*, 374–392. [[CrossRef](#)]
25. Ivanova, N.; Pedersen, L.T.; Tonboe, R.T.; Kern, S.; Heygster, G.; Lavergne, T.; Sørensen, A.; Saldo, R.; Dybkjær, G.; Brucker, L.; et al. Inter-Comparison and Evaluation of Sea Ice Algorithms: Towards Further Identification of Challenges and Optimal Approach Using Passive Microwave Observations. *Cryosphere* **2015**, *9*, 1797–1817. [[CrossRef](#)]
26. Lavergne, T.; Sørensen, A.M.; Kern, S.; Tonboe, R.; Notz, D.; Aaboe, S.; Bell, L.; Dybkjær, G.; Eastwood, S.; Gabarro, C.; et al. Version 2 of the EUMETSAT OSI SAF and ESA CCI Sea-Ice Concentration Climate Data Records. *Cryosphere* **2019**, *13*, 49–78. [[CrossRef](#)]
27. Cavalieri, D.J. A Microwave Technique for Mapping Thin Sea Ice. *J. Geophys. Res. Ocean.* **1994**, *99*, 12561–12572. [[CrossRef](#)]
28. Kwok, R.; Comiso, J.C.; Martin, S.; Drucker, R. Ross Sea Polynyas: Response of Ice Concentration Retrievals to Large Areas of Thin Ice. *J. Geophys. Res. Ocean.* **2007**, *112*, C03S21. [[CrossRef](#)]
29. Shokr, M.; Kaleschke, L. Impact of Surface Conditions on Thin Sea Ice Concentration Estimate from Passive Microwave Observations. *Remote Sens. Environ.* **2012**, *121*, 36–50. [[CrossRef](#)]
30. Barber, D.G.; Fung, A.K.; Grenfell, T.C.; Nghiem, S.V.; Onstott, R.G.; Lytle, V.I.; Perovich, D.K.; Gow, A.J. The Role of Snow on Microwave Emission and Scattering over First-Year Sea Ice. *IEEE Trans. Geosci. Remote Sens.* **1998**, *36*, 1750–1763. [[CrossRef](#)]
31. Nihashi, S.; Ohshima, K.I.; Tamura, T.; Fukamachi, Y.; Saitoh, S. Thickness and Production of Sea Ice in the Okhotsk Sea Coastal Polynyas from AMSR-E. *J. Geophys. Res. Ocean.* **2009**, *114*, C10025. [[CrossRef](#)]
32. Shokr, M.; Asmus, K.; Agnew, T.A. Microwave Emission Observations from Artificial Thin Sea Ice: The Ice-Tank Experiment. *IEEE Trans. Geosci. Remote Sens.* **2009**, *47*, 325–338. [[CrossRef](#)]
33. Similä, M.; Mäkynen, M.; Karvonen, J.; Gegicu, A.; Gierisch, A. Modeled Sea Ice Thickness Enhanced by Remote Sensing Data. In Proceedings of the Proc. European Space Agency Living Planet Symposium, Prague, Czech Republic, 9–13 May 2016; ESA: Prague, Czech Republic, 2016. Volume ESA SP-740. p. 6.
34. Mäkynen, M.; Cheng, B.; Similä, M. On the Accuracy of Thin-Ice Thickness Retrieval Using MODIS Thermal Imagery over Arctic First-Year Ice. *Ann. Glaciol.* **2013**, *54*, 87–96. [[CrossRef](#)]
35. Mäkynen, M.; Karvonen, J. MODIS Sea Ice Thickness and Open Water–Sea Ice Charts over the Barents and Kara Seas for Development and Validation of Sea Ice Products from Microwave Sensor Data. *Remote Sens.* **2017**, *9*, 1324. [[CrossRef](#)]
36. JCOMM Expert Team on Sea Ice. *Sea-Ice Nomenclature: Snapshot of the WMO Sea Ice Nomenclature WMO No. 259, Volume 1—Terminology and Codes*; WMO-JCOMM: Geneva, Switzerland, 2014.
37. Comiso, J.C.; Cho, K. “Description of GCOM-W1 AMSR2 Sea Ice Concentration Algorithm,” in “Descriptions of GCOM-W1 AMSR2 Level 1R and Level 2 Algorithms”; Japan Aerospace Exploration Agency, Earth Observation Research Center: Tsukuba, Japan, 2013.
38. OSI SAF. *Global Sea Ice Type (netCDF)—Multimission*; EUMETSAT SAF on Ocean and Sea Ice: Darmstadt, Germany, 2017.
39. Yang, H.; Zou, X.; Li, X.; You, R. Environmental Data Records from FengYun-3B Microwave Radiation Imager. *IEEE Trans. Geosci. Remote Sens.* **2012**, *50*, 4986–4993. [[CrossRef](#)]
40. Hersbach, H.; Bell, B.; Berrisford, P.; Biavati, G.; Horányi, A.; Muñoz Sabater, J.; Nicolas, J.; Peubey, C.; Radu, R.; Rozum, I.; et al. ERA5 Hourly Data on Single Levels from 1979 to Present. *Copernic. Clim. Chang. Serv. (C3S) Clim. Data Store (CDS)* **2018**, *10*, 24381.
41. Hersbach, H.; Bell, B.; Berrisford, P.; Hirahara, S.; Horányi, A.; Muñoz-Sabater, J.; Nicolas, J.; Peubey, C.; Radu, R.; Schepers, D.; et al. The ERA5 Global Reanalysis. *Q. J. R. Meteorol. Soc.* **2020**, *146*, 1999–2049. [[CrossRef](#)]

42. Tian-Kunze, X. *SMOS Sea Ice Thickness Product Description Document (PDD), Issue 3.0*; Alfred Wegener Institute: Bremerhaven, Germany, 2021.
43. Tian-Kunze, X. *SMOS Sea Ice Thickness ReadMe-First Technical Note (RM-TN), Issue 2.0*; Alfred Wegener Institute: Bremerhaven, Germany, 2021.
44. NSIDC A Guide to NSIDC's Polar Stereographic Projection. Available online: <https://nsidc.org/data/user-resources/help-center/guide-nsidcs-polar-stereographic-projection> (accessed on 20 July 2023).
45. Wentz, F.J.; Meissner, T. *AMSR Ocean Algorithm, Algorithm Theoretical Basis Document (ATBD)*; Remote Sensing Systems: Santa Rosa, CA, USA, 2000.
46. Tian, T.; Tonboe, R.; Lavelle, J. *The EUMETSAT OSI SAF AMSR-2 Sea Ice Concentration Algorithm, Algorithm Theoretical Basis Document, Product OSI 408*; EUMETSAT OSI SAF: Darmstadt, Germany, 2015; p. 20.
47. Tonboe, R.T.; Eastwood, S.; Lavergne, T.; Sørensen, A.M.; Rathmann, N.; Dybkjær, G.; Pedersen, L.T.; Høyer, J.L.; Kern, S. The EUMETSAT Sea Ice Concentration Climate Data Record. *Cryosphere* **2016**, *10*, 2275–2290. [[CrossRef](#)]
48. Mathew, N.; Heygster, G.; Melsheimer, C. Surface Emissivity of the Arctic Sea Ice at AMSR-E Frequencies. *IEEE Trans. Geosci. Remote Sens.* **2009**, *47*, 4115–4124. [[CrossRef](#)]
49. Cavalieri, D.J.; Crawford, J.P.; Drinkwater, M.R.; Eppler, D.T.; Farmer, L.D.; Jentz, R.R.; Wackerman, C.C. Aircraft Active and Passive Microwave Validation of Sea Ice Concentration from the Defense Meteorological Satellite Program Special Sensor Microwave Imager. *J. Geophys. Res.* **1991**, *96*, 21989–22008. [[CrossRef](#)]
50. Shi, L.; Liu, S.; Shi, Y.; Ao, X.; Zou, B.; Wang, Q. Sea Ice Concentration Products over Polar Regions with Chinese FY3C/MWRI Data. *Remote Sens.* **2021**, *13*, 2174. [[CrossRef](#)]
51. Afanasyeva, E.; Alekseeva, T.A.; Sokolova, J.V.; Demchev, D.M.; Chufarova, M.S.; Bychenkov, Y.U.; Devyataev, D.V. AARI Methodology for Sea Ice Charts Composition. *Russ. Arct.* **2019**, *7*, 5–20. [[CrossRef](#)]
52. Melsheimer, C.; Spreen, G.; Ye, Y.; Shokr, M. First Results of Antarctic Sea Ice Type Retrieval from Active and Passive Microwave Remote Sensing Data. *Cryosphere* **2023**, *17*, 105–126. [[CrossRef](#)]

Disclaimer/Publisher's Note: The statements, opinions and data contained in all publications are solely those of the individual author(s) and contributor(s) and not of MDPI and/or the editor(s). MDPI and/or the editor(s) disclaim responsibility for any injury to people or property resulting from any ideas, methods, instructions or products referred to in the content.